Supplementary Information for:

Revisiting Metal Fluorides as Lithium-ion Battery Cathodes

Xiao Hua[1,2, 3], Alexander S. Eggeman[4,5], Elizabeth Castillo-Martínez[1,6], Rosa Robert[1], Harry S. Geddes[3], Ziheng Lu[4], Chris J. Pickard[4,7], Wei Meng[1], Kamila M. Wiaderek[8], Nathalie Pereira[9], Glenn G. Amatucci[9], Paul A. Midgley[4], Karena W. Chapman[8,10], Ullrich Steiner[2], Andrew L. Goodwin[3], and Clare P. Grey[1*]*

1: Department of Chemistry, University of Cambridge, Lensfield Road, Cambridge, CB2 1EW, United Kingdom
2: Adolphe Merkle Institute, Chemin des Verdiers 4, 1700 Fribourg, Switzerland
3: Inorganic Chemistry Laboratory, University of Oxford, South Parks Road, Oxford OX1 3QR, United Kingdom
4: Department of Materials Science and Metallurgy, University of Cambridge, Pembroke Street, Cambridge CB2 3QZ, United Kingdom
5: Department of Materials, University of Manchester, Manchester M13 9PL, United Kingdom
6: Departamento Química Inorgánica, Universidad Complutense de Madrid, 28040 Madrid, Spain
7: Advanced Institute for Materials Research, Tohoku University, Sendai, Japan
8: X-ray Science Division, Advanced Photon Source, Argonne National Laboratory, Argonne, Illinois 60439, United States
9: Energy Storage Research Group, Department of Materials Science and Engineering, Rutgers University, North Brunswick, New Jersey 08902, United States
10: Department of Chemistry, SUNY Stony Brook, Stony Brook, NY 11790-3400, United States

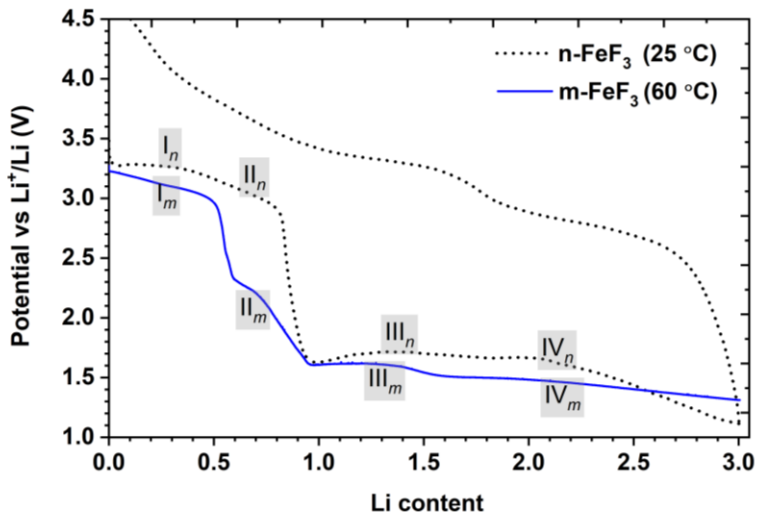

Figure S1. Comparison of the galvanostatic profiles of m-FeF_3's discharge process at 60℃ (blue solid) and n-FeF_3's full cycle at 25℃ (black dotted). Both measurements were performed using a current rate of C/100. We note that it is difficult to charge m-FeF_3 even at the higher temperatures. Lithiation processes (I-IV) associated with FeF_3 are labelled on the voltage profile with the corresponding illustrated scheme shown in Figure 5d of the main text. Process (V), which results from the extruded FeF_2, is omitted for clarity. Subscripts *n* and *m* respectively denote the processes for n- and m-FeF_3. The most prominent difference in voltage profiles between these two materials lies in process II, where m-FeF_3 shows a lower and more sloping voltage. This distinct voltage profile of m-FeF_3 is likely due to an increased overpotential associated with the nucleation and movement of the *A*-*B* phase boundary in the two-phase reaction in the larger particle. Process II in n-FeF_3 exhibits a solid-solution behaviour, and this reaction does not involve such a phase boundary, in turn leading to a smaller overpotential.

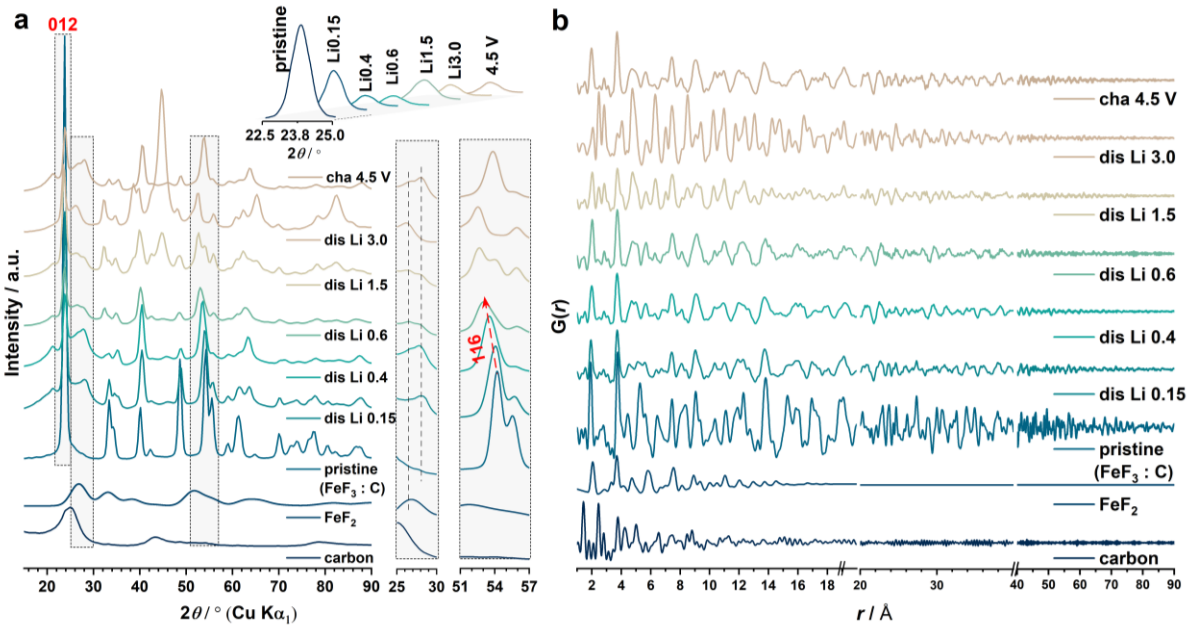

Figure S2. X-ray total scattering data of selected m-FeF_3 samples showing **a)** (low-resolution) XRD patterns and **b)** their corresponding PDF patterns. Simulations of n-FeF_2 (2 nm) and experimental data for carbon are also shown for comparison. The intensity reduction of the (012) reflection, peaks within 25° - 30° 2θ, and the shifts of the (116) reflection are highlighted in the insets.

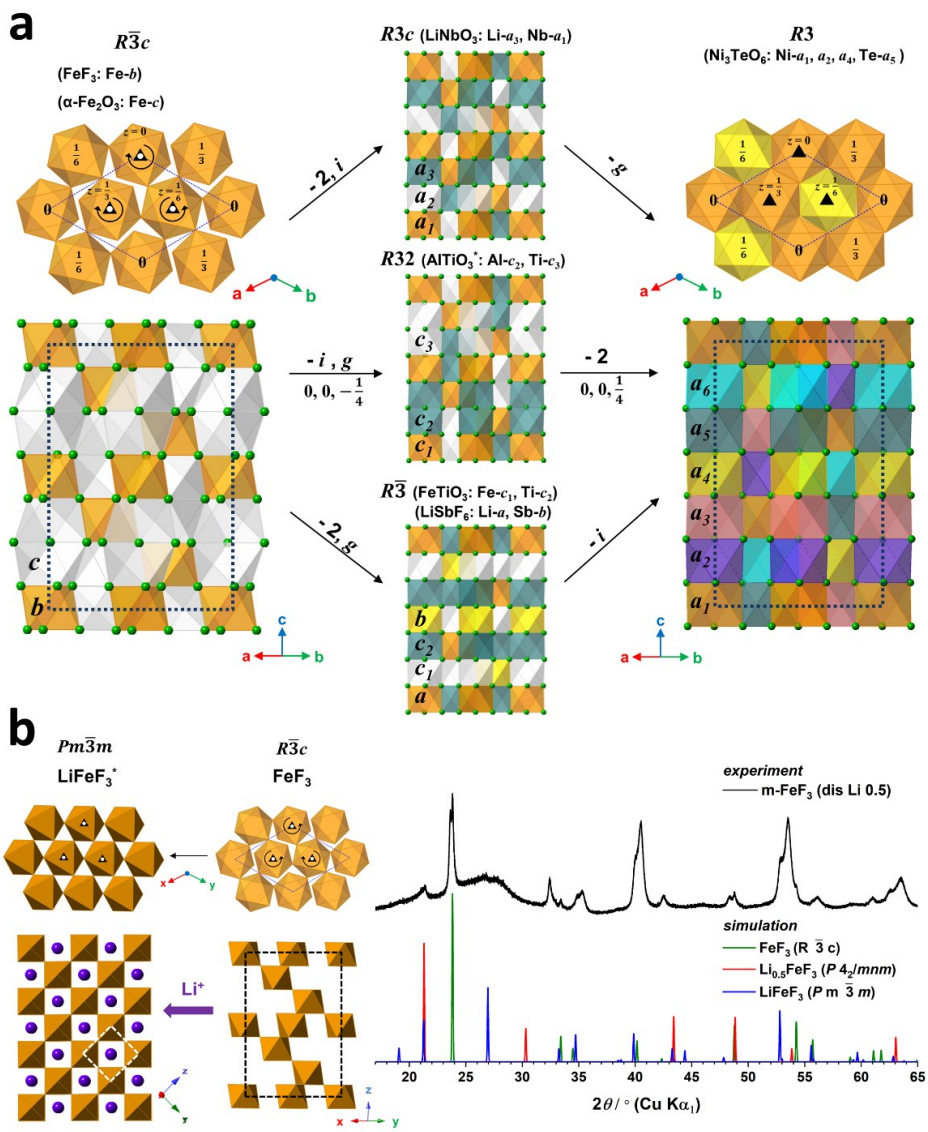

Figure S3. a) Hettotypes of ABX_3 ($R\bar{3}c$) structure. The same colours in each structure shows equivalent positions with the corresponding Wyckoff letters marked, e.g. "FeF_3: Fe-b" corresponds to the FeF_3 structure in which Fe occupies the *b* sites. A symmetry lowering from $R\bar{3}c$ to *R*3 can occur via three distinct intermediate structures shown in the middle. Particularly, in *R*3 symmetry, the sites in brown (a_1) and yellow (a_4) form a corner-shared octahedral network, the same as the FeF_6-framework in the original FeF_3 structure. "2", "*i*" and "*g*" stand for two-fold symmetry, inversion, and *c*-glide, respectively. (0,0, ±1/4) stands for the vector for origin shift. The projection of the structure viewed along the [001] zone axis, showing the 3-fold rotation axis passing through the Fe octahedra (where each Fe has their relative position along the *c*-axis and inversion centre position marked). Rotation about this axis allows the structure to transform into a perfect *hcp* anion packing. The corresponding direction of each 3-fold rotation required to complete this transformation is also marked. **b)** Aristotype (cubic perovskite) of ABX_3 ($R\bar{3}c$) structure. Note that another aristotype $P6_3/mmc$ structure (hexagonal perovskite) is not discussed here because its transformation to $R\bar{3}c$ corresponds to a non-executable transition involving changes of chemical composition that cannot be obtained via a simple structure distortion[1]. Symbol "*" indicates that the structure is hypothetically constructed. Dashed lines show the unit cells. Experimental HRXRD pattern of the "dis Li 0.5" m-FeF_3 sample is shown and compared with simulations of FeF_3, $Li_{0.5}FeF_3$ (trirutile), and $LiFeF_3$ (cubic perovskite based on $KFeF_3$). We also note the Goldsmith's tolerance factor for the perovskite-related Li_xFeF_3 is around 0.70[2], below what is expected for stable perovskites.

Section S1. Initial XRD refinement

In the *R*3 structure, two F and six Fe atoms are located at 9*b* and 3*a* sites, respectively. In the initial refinement, a partial and equal Fe occupancy (33%) in all of the *a* sites (Fig. 1c) was chosen for a starting point for our refinements for both *A*- and *B*-$Li_xFe_yF_3$ given the reported migration of Fe atoms[3], but with no prior information concerning their actual positions and the extent of migration. In addition, Li atoms were ignored due to their small X-ray scattering power (cf. Fe) and low concentration (cf. F); the broad feature (at 26 - 28° 2θ) was treated as a scattering background whose physical nature will be explored later. According to the result of the refinement, the Fe occupancies of these six *a* sites ($f_{a_n}^{Fe}, n = 1\sim6, f$ for fractional occupancy) in *B*-$Li_xFe_yF_3$ indicate an *R*3c symmetry, that is $f_{a_1} \approx f_{a_4} \not\approx 0, f_{a_3} \approx f_{a_6} \not\approx 0, f_{a_2} \approx f_{a_5} \approx 0$; whereas the $f_{a_n}^{Fe}$ for *A*-$Li_xFe_yF_3$ ($f_{a_1} \not\approx f_{a_2} \not\approx f_{a_3} \not\approx f_{a_4} \not\approx f_{a_5} \not\approx f_{a_6} \not\approx 0$) does not imply any higher-symmetry space group.

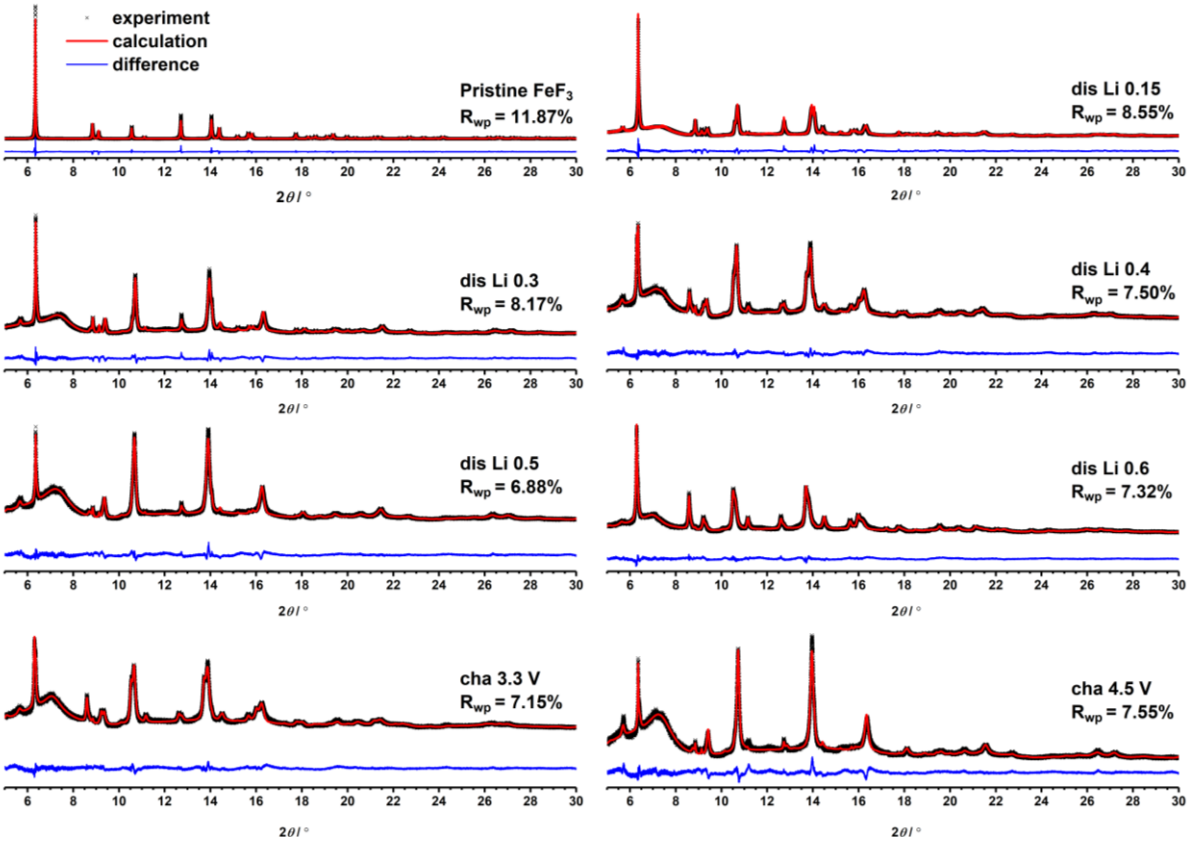

Figure S4. Rietveld refinement of the HRXRD data (λ = 0.4138 Å) from m-FeF_3 samples collected at different states of charge. The experimental, calculated and difference patterns are shown in black crosses, red and blue lines, respectively. The derived contribution of each phase and its molar fraction are shown in Fig. 2b and their lattice parameters are shown in Fig. S5. Note that the broad features between 6° − 8° 2θ seen in all the cycled samples are treated as background.

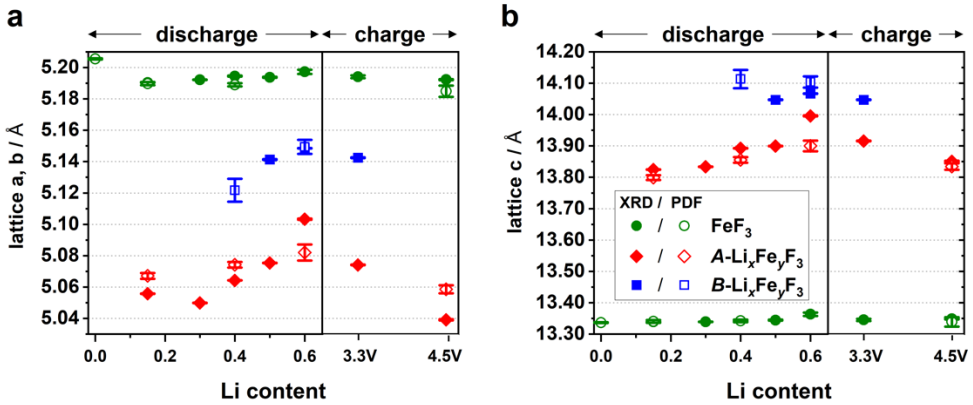

Figure S5. Evolution of lattice parameters **a)** *a* / *b* and **b)** *c* for FeF_3 (green circle), *A*-$Li_xFe_yF_3$ (red diamond) and *B*-$Li_xFe_yF_3$ (blue square) derived from HRXRD (filled) and XPDF (hollow) refinements (Fig. 2, S4 and S6).

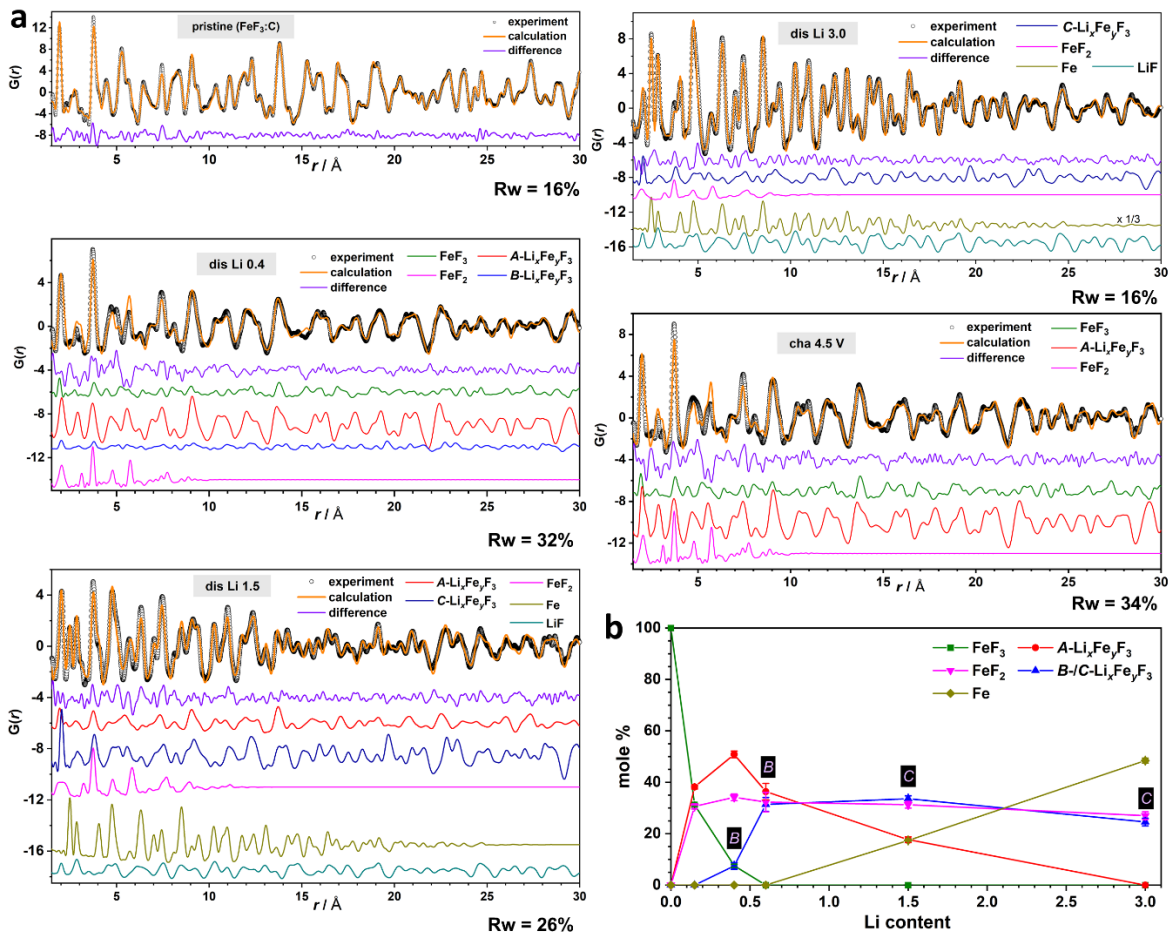

Figure S6. a) XPDF refinement of selected m-FeF_3 samples with experimental, calculated and difference patterns shown in black circles, orange and purple lines respectively. Contributions from each component are also shown including FeF_3 (green), FeF_2 (pink), *A*-$Li_xFe_yF_3$ (red), *B*-/*C*-$Li_xFe_yF_3$ (blue/dark blue), Fe (dark yellow) and LiF (cyan). **b)** Discharge phase evolution derived from XPDF refinement.

Section S2. Charge-flipping

The intensities of the *0kl* reflections for the *A*-$Li_xFe_yF_3$ material were extracted from the precession ED pattern recorded parallel to the [100] zone-axis of the sample "dis Li 0.25". In order to estimate the projected atomic structure along this direction a structure solution was attempted using a charge-flipping algorithm. Friedel symmetry was enforced and the flipping threshold was set at +0.1 standard deviations from the mean value of the density. 50 runs were performed and the stable solution in each case saved. The only estimate to appear repeatedly in this set (12 times) was the result reported in the manuscript.

Section S3. Scanning Electron Diffraction

A full diffraction pattern is recorded for the "dis Li 0.25" sample at each point of a raster across the sample with a step size of 2.5 nm. The signal at each scan position can then be analysed offline to recover the structure and orientation giving rise to each individual pattern[4]. Every pattern underwent a comparison against pre-generated libraries of diffraction patterns for pristine FeF_3 and lithiated *A*-$Li_xFe_yF_3$ structures.

Section S4. ED analysis of *B*-$Li_xFe_yF_3$

The structure of *B*-$Li_xFe_yF_3$ was investigated against the "dis Li 0.6" sample whose pattern (Fig. S7a) shows distinct reflections compared to that of *A*-$Li_xFe_yF_3$. While the strong reflections are consistent to the simulated pattern (Fig. S7b) using the XRD-derived $R3c$ structure, some additional weak reflections indexed to the $\{0\ k\ l\}$-type ($l = 2n + 1$) can also be observed (Fig. S8c). These reflections, i.e., (003) and (01-1), are forbidden by the *c*-glide plane implying a slight distortion from the *R*3c symmetry. Importantly, these reflections are consistent with the observation made earlier in XRD data (Fig. 2a).

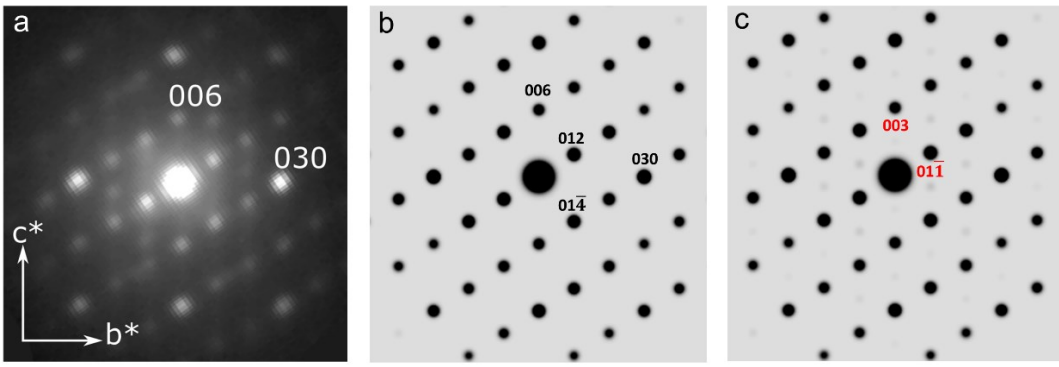

Figure S7. a) ED pattern of "dis Li 0.6" m-FeF_3 sample recorded from the [100] zone axis. **b)** Simulated ED pattern using the *B*-$Li_xFe_yF_3$ ($R3c$) structure derived from the HRXRD refinement. **c)** Simulated ED pattern using a modified *B*-$Li_xFe_yF_3$ structure (*R*3) whose symmetry slightly deviates from *R*3c by a 2% difference in the Fe occupancy of the Fe sites.

Section S5. DFT calculations

Based on our analysis, a structure nearly identical to that proposed from electron diffraction studies was found in two slightly different forms. The first is a monoclinic (*C*2) distortion of the rhombohedral FeF_3 structure (leading to a larger unit cell and a larger number of atoms in the asymmetric subunit), while the second was based on the ED solution albeit with a higher symmetry of *P*312 (this structure is detailed in Table S1). Both structures were found to have a free energy within 0.03eV/f.u. of the trirutile structure indicating their relative stability and importantly both structures showed the same stacking sequence with alternating layers of Fe^{2+} and Fe^{3+} along the *c*-axis of the structure, leading to a weak ferrimagnetic or antiferromagnetic response overall. The Li positions were found to be ordered into layers with the Fe^{3+} ions, while the exact positions within the layer may not be correct, the high mobility of the Li^{+} should allow for a range of possible locations. It is important to note that Li itself does not account for the change in symmetry and structure of the crystal, but instead the indirect effect of Li on the Fe oxidation state and ordering in the lattice that determines the final crystal structure.

Table S1. Table of atomic positions and spin states in the *P*312 structure.

Atom	Occ.	*x*	*y*	*z*	Spin (*ħ*/2)
Fe1	1.000	2/3	1/3	0.1602	3.87
Fe2	1.000	2/3	1/3	0.8398	3.87
Fe3	1.000	1/3	2/3	0.3278	-4.31
Fe4	1.000	1/3	2/3	0.0000	-4.32
Fe5	1.000	1/3	2/3	0.6722	-4.31
Fe6	1.000	0.0000	0.0000	0.5000	3.82
F1	1.000	0. 6555	-0.0151	0.0760	-0.09
F2	1.000	0.6728	0.9488	0.4027	-0.10
F3	1.000	0.6459	0.6582	0.2462	-0.08
F4	1.000	0.0151	0.3445	0.9240	-0.09
F5	1.000	0.0512	0.3272	0.5973	-0.10
F6	1.000	0.3418	0.3541	0.7538	-0.08
Li1	1.000	0.0000	0.0000	0.0000	0.01
Li2	1.000	0.0000	0.0000	0.6999	0.00
Li3	1.000	0.0000	0.0000	0.3001	0.00

Table S2. DFT calculation results.

Formula	Space Group	Pressure/ GPa	Volume/ $Å^3$	Relative Enthalpy per fu/eV	Integrated spin	Integrated |spin|	#fu
$LiFe_2F_6$	*Cmmm*	0.06	108.226	0.000	-0.99	8.72	2
$LiFe_2F_6$	*C*2	0.06	110.406	0.053	-1.00	8.63	3
$LiFe_2F_6$	$P4_2/mnm$	-0.00	107.582	0.082	-0.00	8.64	2
$LiFe_2F_6$	P312	0.02	109.894	0.102	-1.00	8.64	3
$LiFe_2F_6$	*P*312	-0.01	109.884	0.104	-1.00	8.64	3

Section S6. SQUID magnetometry data

Fig. S8 shows the magnetic susceptibility data of pristine m-FeF_3 and "dis Li 0.4" sample (both containing carbon). FeF_3 orders antiferromagnetically (AFM) at T_N = 353 K[5]. Deviation between FC and ZFC due to the FM component is seen in the susceptibility curves at all measured temperatures (2 - 300K). Because of the magnetic order the inverse of susceptibility cannot really be fitted to Curie Weiss law, as the material is not in the paramagnetic regime. For "dis Li 0.4" sample, the FC and ZFC are also different in all temperature range. This is probably due to residual FeF_3, as shown in the PXRD data. Below 300K there is a new anomaly at approx. 100 K. The susceptibility values suggest that the ground state in *A*-$Li_xFe_yF_3$ is also antiferromagnetic. The enhanced splitting between FC and ZFC curves below 100 K suggests there is a weak canting also in this phase, although it is also consistent with the presence of FeF_2 which orders AFM below T_N = 78 K. Magnetisation vs applied magnetic field (H) at 200K, above the temperature for magnetic ordering of *A*-$Li_xFe_yF_3$, shows that the saturation and remanent magnetizations due to FeF_3 are approximately 20% in "dis Li 0.4", suggesting that 20% m-FeF_3 is left. This qualitatively agrees with new phase having the composition of *A*-$Li_{0.5}FeF_3$. (The approximate FeF_3 contents in "dis Li 0.4" are about 5% and 7% according the HRXPD (Fig. 2) and PDF (Fig. 3) refinements, respectively.)

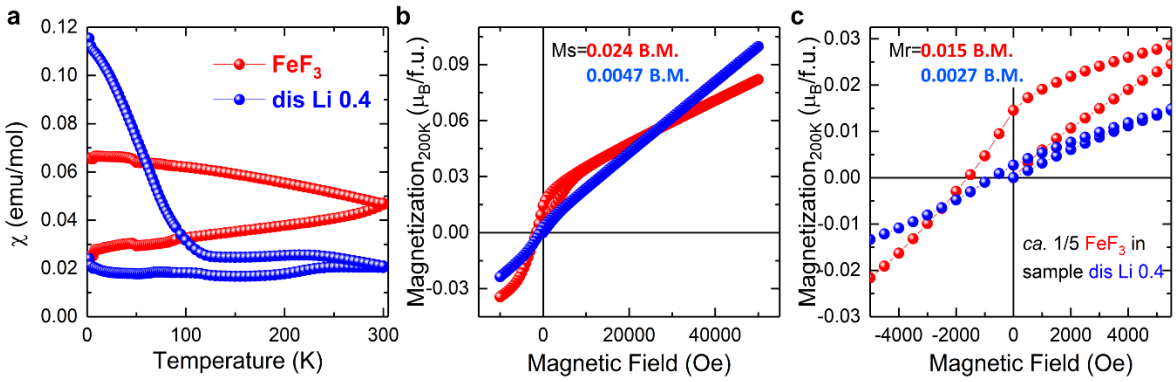

Figure S8. Magnetic properties of m-FeF_3 (red) and "dis Li 0.4" m-FeF_3 sample (blue) **a)** Magnetic susceptibility vs temperature, ZFC and FC (100 Oe) **b)** Magnetization vs applied magnetic field at 200 K and **c)** zoom near the zero magnetic field region showing the remanent magnetization.

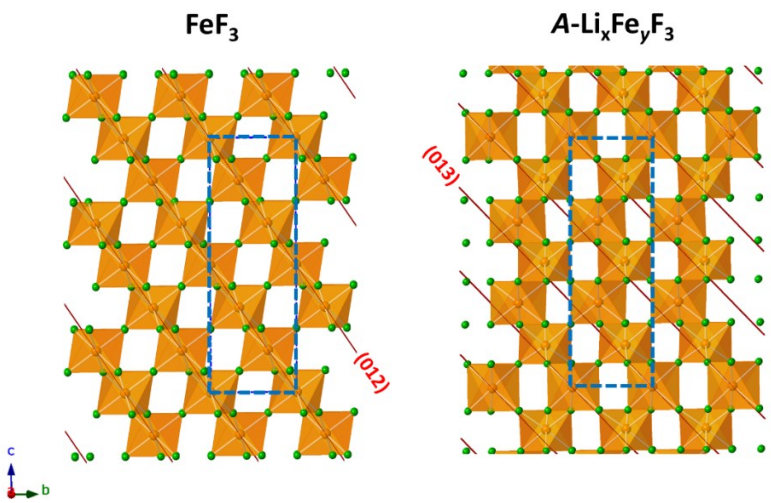

Figure S9. Comparison between the (012) planes in FeF_3 ($R\bar{3}c$) and the (013) planes in *A*-$Li_xFe_yF_3$ ($P312$) that give rise to the highest intensity reflections in their respective diffraction patterns. Unit cells are indicated by the blue dashed line.

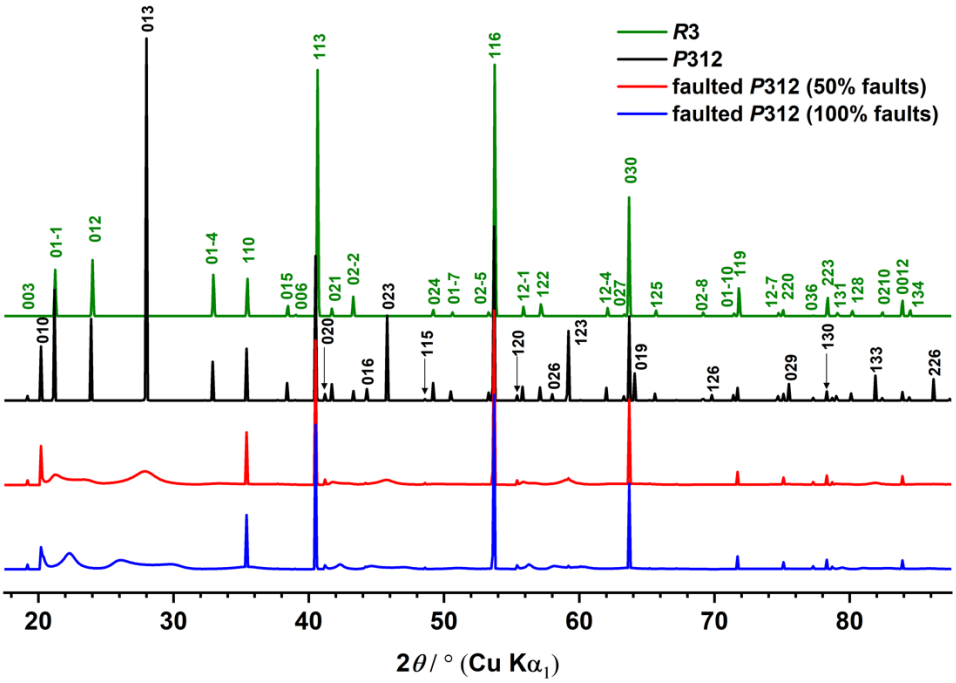

Figure S10. XRD patterns of A-$Li_xFe_yF_3$ computed from HRXRD-derived $R3$ structure (green) and faulted model based on the ED-derived $P312$ cell as the stacking unit containing 0% (black), 50% (red) and 100% (blue) faults. Between the $R3$ and $P312$ XRD patterns, common reflections are labelled in green while new reflections emerged from the primitive trigonal symmetry are labelled in black. The stacking faults result in a notable intensity reduction and peak broadening for all the (01l) and (02l) reflections (consistent with ED simulation in Fig. S12). Of particular importance, the (013) peak has a position in line with the background-like feature at 28.0° 2θ observed in our experimental XRD.

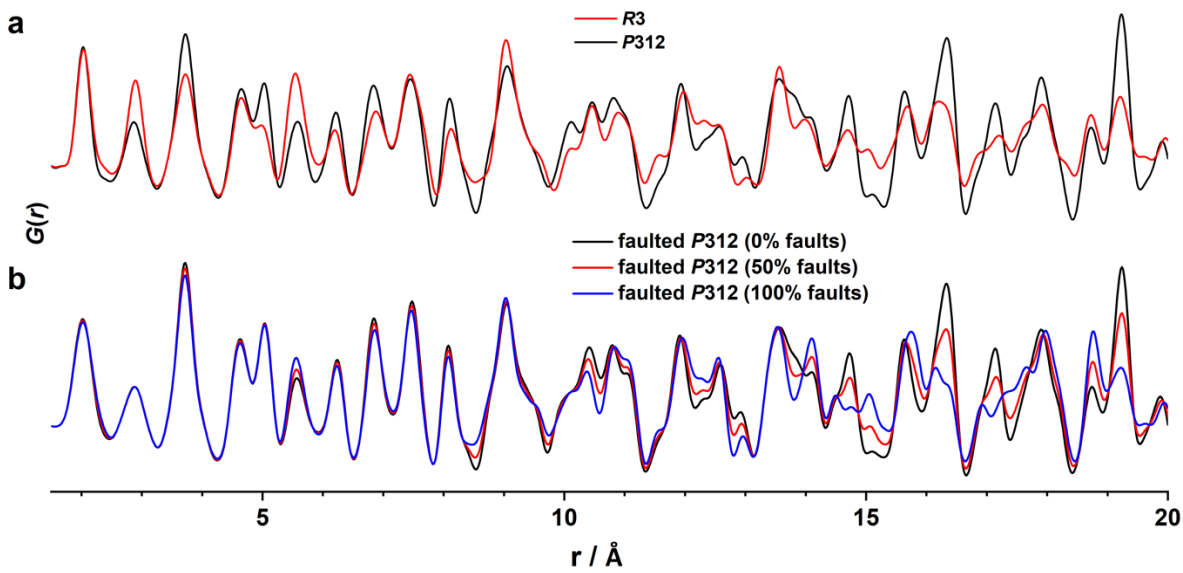

Figure S11. a) PDF simulation of A-$Li_xFe_yF_3$ using HRXRD-derived $R3$ structure (red) in comparison with the simulation using ED-derived $P312$ cell (black). **b)** Comparison of the PDF simulation using the $P312$ structure incorporating 0% (black), 50% (red) and 100% (blue) stacking faults. The few changes in peak intensities at low r ($r < 5$ Å) suggest the insensitivity of the local structure to the stacking disorder. Therefore, the observed intensity discrepancy for atom pairs at 2.9 and 3.7 Å in a) − which respectively correspond to edge- and corner-shared Fe-Fe interatomic distances − implies partial migration of corner-shared Fe to edge-shared positions.

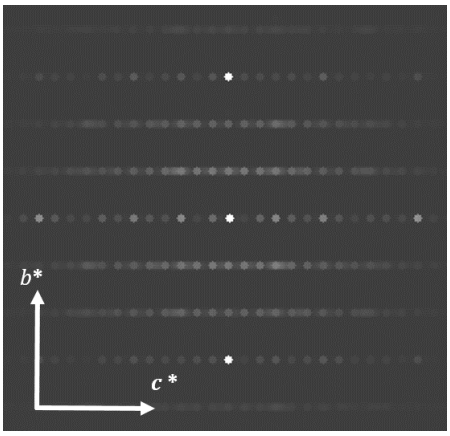

Figure S12. Simulated ED pattern of *A*-$Li_xFe_yF_3$ using faulted *P*312 structure. Note the intensity in the (01*l*) and (02*l*) rows of reflections becomes 'smeared' out along the *c** direction by the stacking disorder. This is consistent with the intensity reduction and peak broadening for the corresponding Bragg reflections observed in the XRD simulation (Fig. S10).

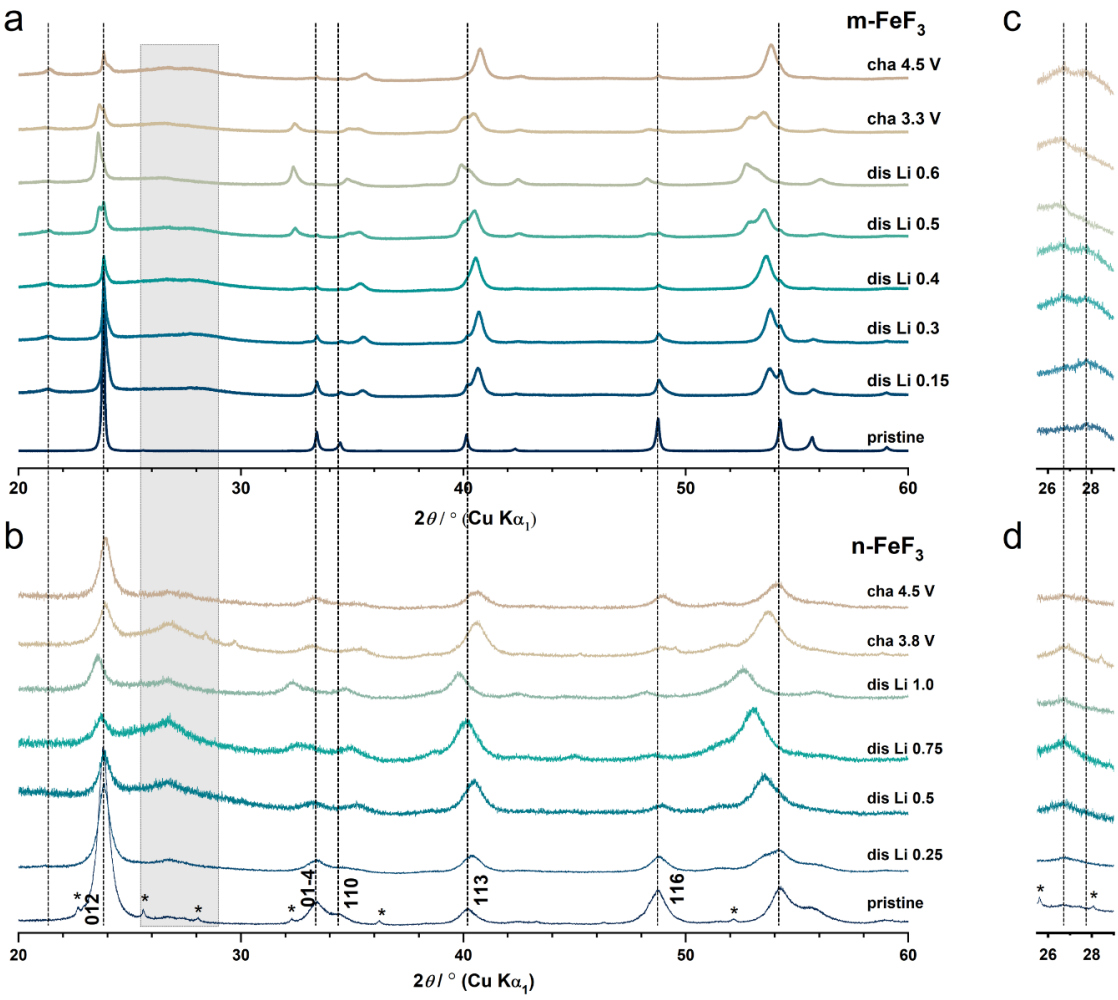

Figure S13. HRXRD patterns for **a)** m-FeF_3 and **b)** n-FeF_3 collected at selected states of charge within the insertion cycle. The shaded region in a) and b) are highlighted in **c)** and **d)**, respectively. Figure a) is a rescaled plot from Figure 2a. Asterisks mark the hydrated FeF_3 impurity introduced during sample preparation. Dotted lines mark the positions of some of the reflections, with the key reflections indexed, to highlight the consistency in the change of diffraction patterns, hence phase behaviours, between m- and n-FeF_3.

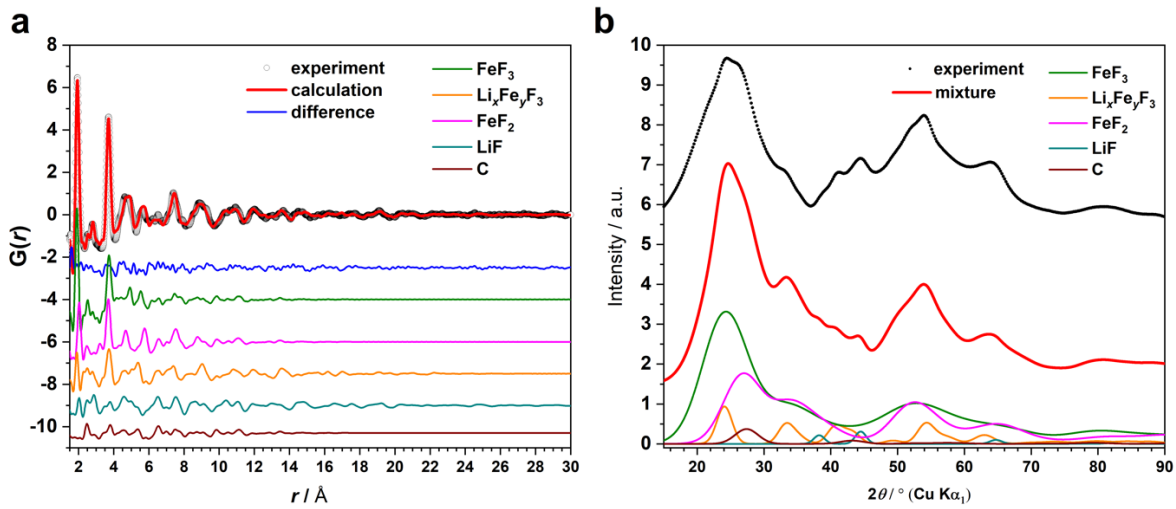

Figure S14. **a)** PDF refinement result of n-FeF_3 collected at the end of 1st charge (4.5 V). Experimental, calculated and difference PDFs are shown in black circle, red and blue lines. PDF contribution from each phase is shown below including FeF_3 (green), FeF_2 (pink), $Li_xFe_yF_3$ (orange), LiF (cyan) and carbon (brown). **b)** The XRD simulation of the various phases derived from PDF refinement shown in (a). The PDF summation from the contribution of each component (red solid) is compared to the experimental pattern (black dotted) which shows excellent agreement (particularly in peak positions), given the highly heterogeneous nature of the sample.

Section S7. Crystal structure of C-$Li_{1+2\eta}Fe_{1-\eta}F_3$ and its formation and further lithiation

The *C*-phase structure was derived from the PDF refinement of m-FeF_3 at the state of "dis Li 1.5" (Fig. S6). The refined structure was further verified in the PDF analysis of the n-FeF_3 series (Fig. 5a and Extended Fig. 1). Note that the real-space analysis is relatively insensitive to symmetry when crystal structures share the same lattice registry, with cation occupancy as the only variable. Hence, we do not exclude other possible space group (Fig. S3) for the *C*-phase. According to the XRD refinement result, the *C*-phase inherits the same structure type (*R*3c) from the parent *B*-phase sharing a similar Fe^{2+} occupancy in the *a*1 site (~ 0.78 and ~ 0.71 for the *B*- and *C*-phase, respectively); however, the *a*3 site, partly occupied by Fe^{2+} in the *B*-phase (~ 0.14), is almost completely empty in the *C*-phase (Fe^{2+} content ~ 0.03).

The close relationship between the *B*- and *C*-phase structures underpins a topotactic *displacement* phase transition (process III) via the removal of Fe^{2+} from the *a*3 site to form Fe^0. This mechanism is also in excellent agreement with the ^{6}Li chemical shift moving towards lower ppm as observed in our previous NMR study (Extended Fig. 1). The further lithiation of the *C*-phase (process IV) triggers the reconstruction of the F^- sublattice from the *hcp* in the *C*-phase to the *fcc* in LiF. No intermediate phase has been observed to date by experiment and no theoretical model has been proposed during this phase transition, thus we conclude that this process proceeds via a *conversion* reaction. Process III and IV take place in parallel with lithiation of FeF_2 (process V), jointly giving rise to Fe nanoparticles (~ 2 nm) embedded in LiF matrix (> 3 nm) at the end of discharge. Given the insulating character and the phase distribution of LiF, the accumulation of this phase results in a gradually increased overpotential at higher Li content (> 2.0), which renders the voltage plateau slope-like.[6] This increased overpotential could consequently leave a trace amount of the *C*-phase unreacted at the end of discharge "Li 3.0", as indicated by our XRD data (Fig. 5b).

Section S8. Mechanisms seen during the charge process

The mechanisms upon the subsequent charge and further cycles were deduced based on our PDF analysis of the n-FeF_3 samples (Extended Fig. 1 and Fig. S15). According to the results, initial delithiation of LiF upon charge consumes the majority of Fe (~ 80 %). Among these reacted Fe, approximately 2/3 of them contribute to forming FeF_2 (~ 2 nm) with the remaining 1/3 reconverted to the *C*-phase via reverse pathway of reaction IV (process IV'). During further delithiation, *C*-$Li_{1+2\eta}Fe_{1-\eta}F_3$ reacts with the residual Fe transforming into *B*-$Li_{1+2\delta}Fe_{1-\delta}F_3$ and *A*-$Li_xFe_{1-\delta}F_3$ successively via *displacement* (III') and *insertion* (II') pathways. The identification of these phases is in good agreement with our previous ^{6}Li NMR study[7] (Extended Fig. 1). When approaching the end of charge (I'), *A*-$Li_xFe_{1-\delta}F_3$ (~ 4 nm) reacts with the adjacent FeF_2 (~ 2 nm) to form FeF_3, whose growth on the particle surface results in passivation in turn inhibiting further delithiation of the *A*-phase. This partial completion of process I' renders the crystallinity of the reformed FeF_3 exceptionally small (~ 1 nm). In addition to this FeF_3, progressively reduced particle sizes were also observed for all other components, collectively giving rise to increasingly broadened diffraction patterns upon delithiation. We also note the remarkably heterogeneous character of the charge reaction whose structure model for refinement requires 5 coexisting phases (Fig. S14). However, despite such heterogeneity, all reaction steps are reversible, meaning that the subsequent lithiation and delithiation processes (Fig. S15) follow analogous pathways to the ones in the first cycle.

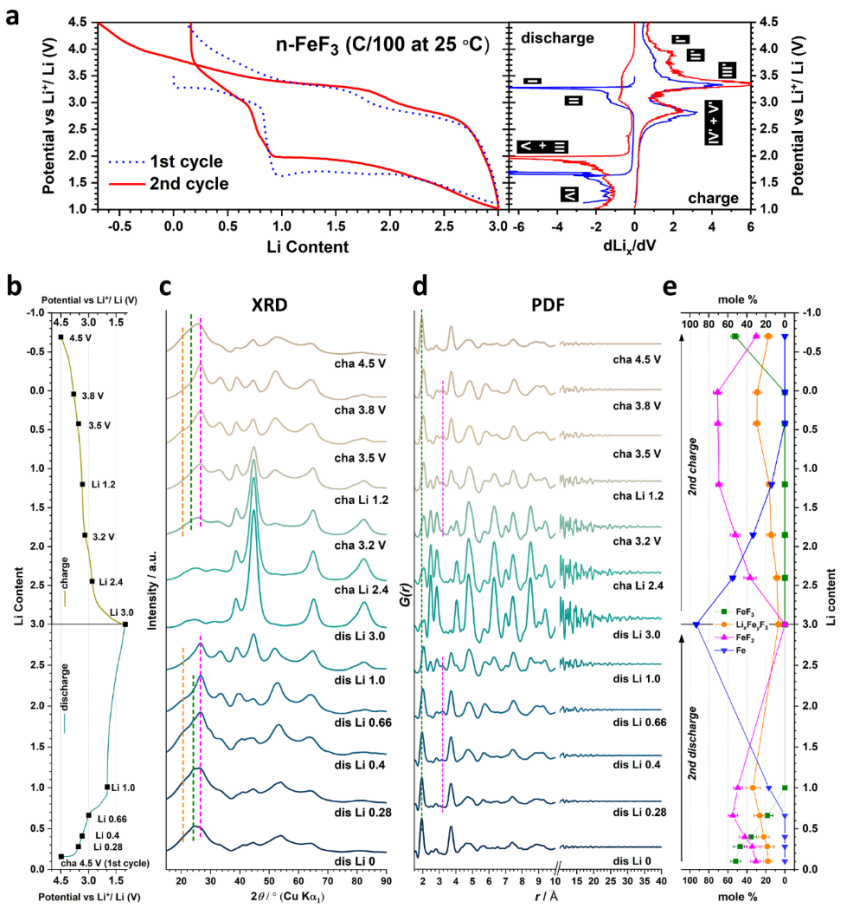

Figure S15. a) Comparison between the 1st (blue dotted) and 2nd (red solid) cycle of n-FeF_3's galvanostatic profile, as well as their respective derivatives (dLi_x/dV), shows identical (de)lithiation processes (highlighted using Roman numerals). **b)** The 2nd discharge and charge galvanostatic profile of n-FeF_3. Black squares mark the selected states of charge where *ex situ* X-ray total scattering experiments were performed to acquire **c)** XRD and **d)** PDF patterns (note that there are two different scales in the *x*-axis). Green, orange and pink dotted lines indicate unique Bragg or PDF features from FeF_3, $Li_xFe_yF_3$ and FeF_2, respectively. **e)** The evolution of the phase mole fractions obtained from the PDF refinement.

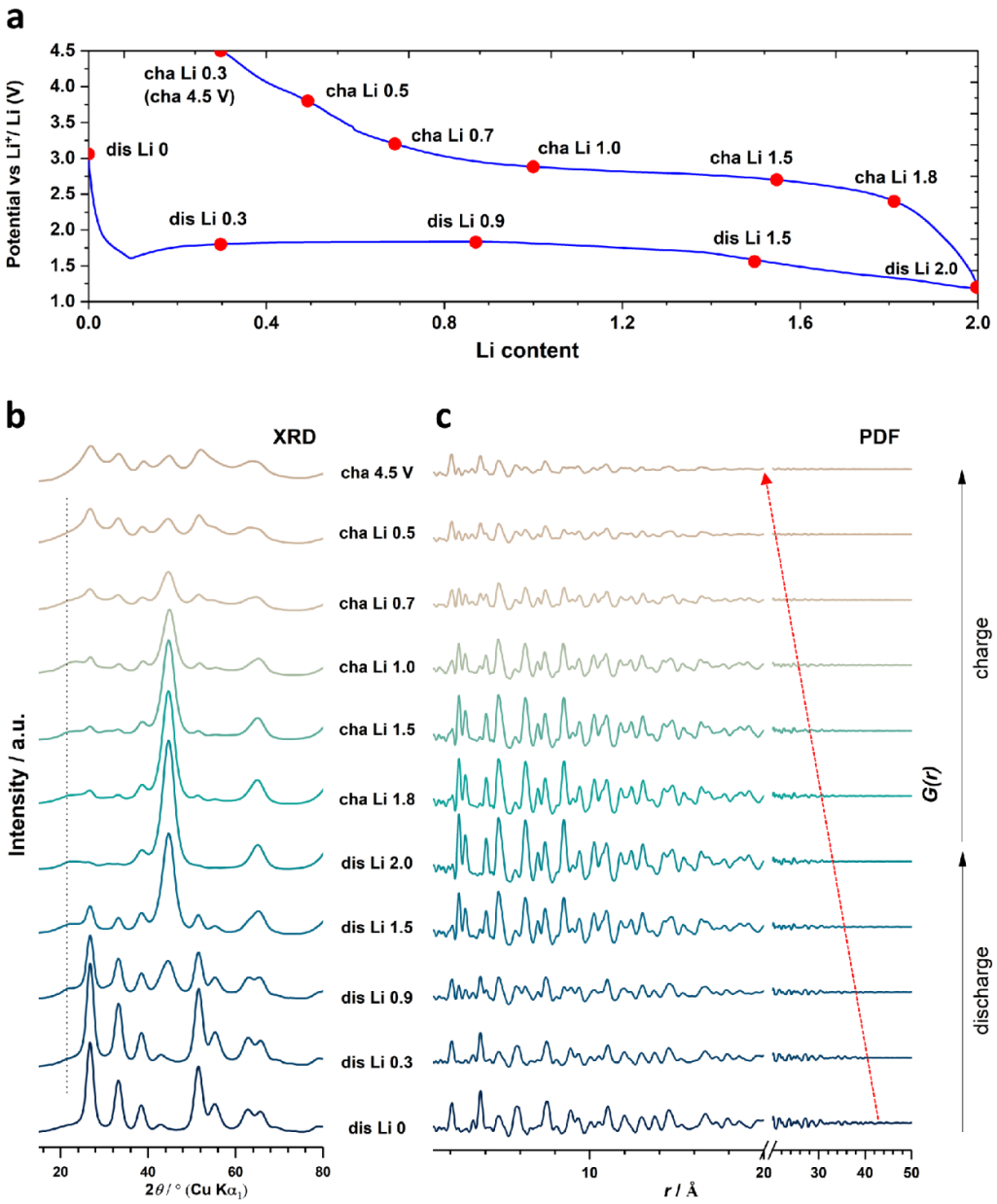

Figure S16. a) The 1st cycle of the galvanostatic profile of FeF_2 (blue). Red circles mark the states of charge where *ex situ* X-ray total scattering experiments were performed to acquire **b)** XRD and **c)** PDF patterns (note that there are two different scales in the *x*-axis). Black dotted line indicates the Bragg feature from intermediate Li_2FeF_4 and the red dashed arrow indicates the reduction in the structure coherence length.

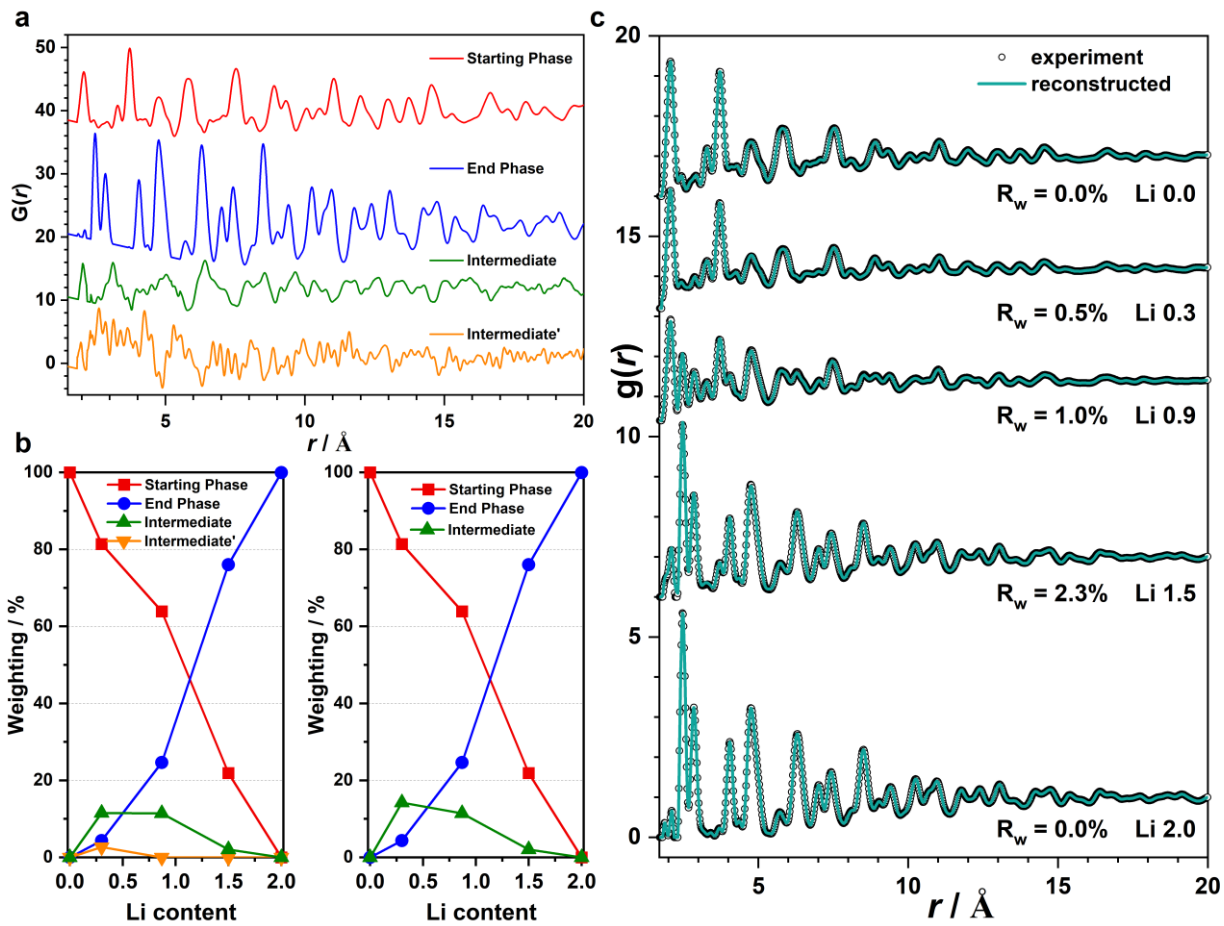

Figure S17. a) Four PDF components derived from the NMF analysis of the PDF data from the 1st discharge: Starting phase (FeF_2), End phase (Fe), Intermediate (Li_2FeF_4) and Intermediate' (likely the artefacts from data treatment). **b)** The respective NMF-derived weightings of the four components and the adjusted weightings with the contribution from the Intermediate' component removed. **c)** Agreement between the experimental data and reconstructed PDF using NMF-derived output, where the Intermediate' component was not included in this analysis, consistent with the proposal that it reflects artifacts.

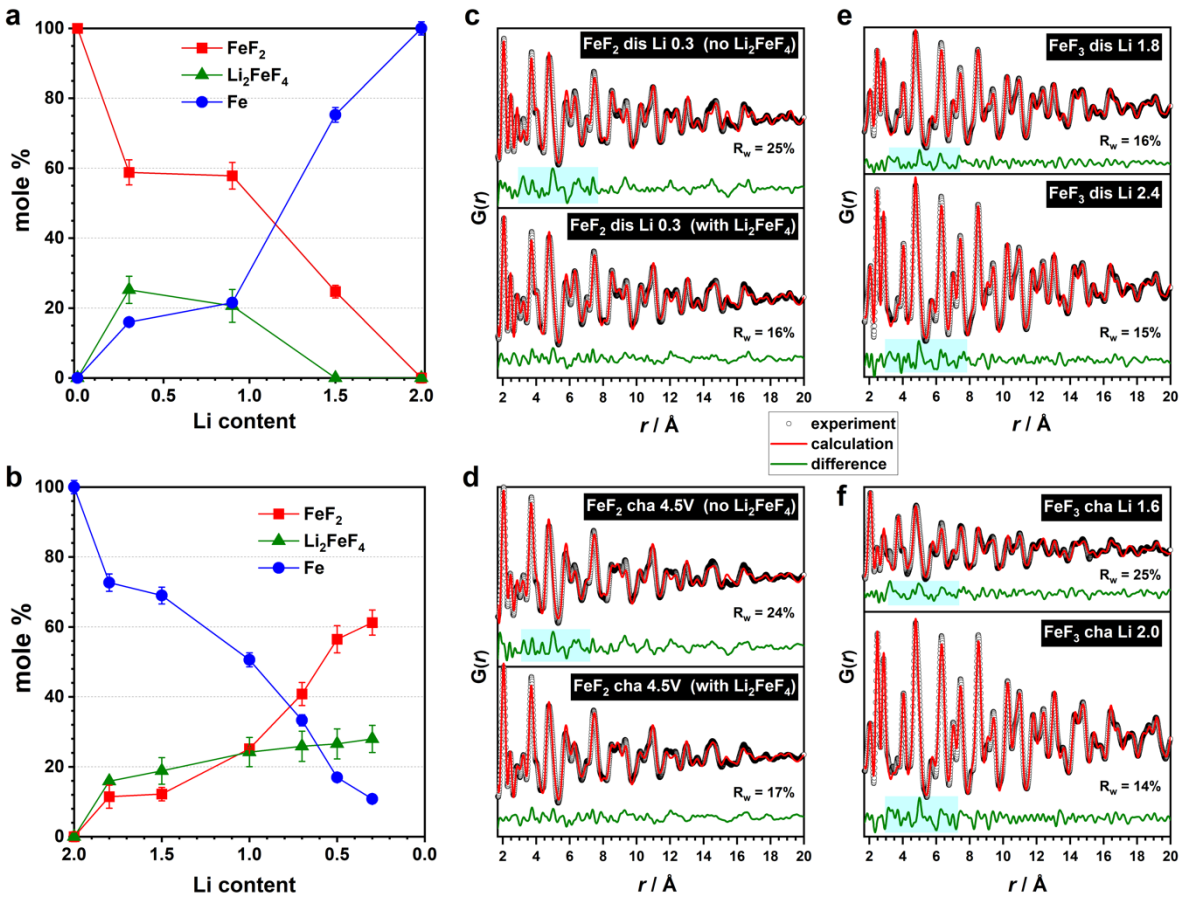

Figure S18. Phase evolution of Fe-containing components derived from refinements of PDF data during **a)** the 1st discharge and **b)** the 1st charge. The phase ratios during discharge are in excellent agreement with the NMF-derived ratios (Fig. S19b). PDF refinements of **c)** "dis Li 0.3" and **d)** "cha 4.5 V" FeF_2 data excluding and including intermediate Li_2FeF_4 structure. The improvement of the fit due to the inclusion of the intermediate is evident. PDF refinements of FeF_3 data during the **e)** 1st discharge and **f)** 1st charge without including intermediate in the structure model. The discernible features due to the exclusion of the intermediate are highlighted in blue boxes.

Section S9. Energy study of the interface model

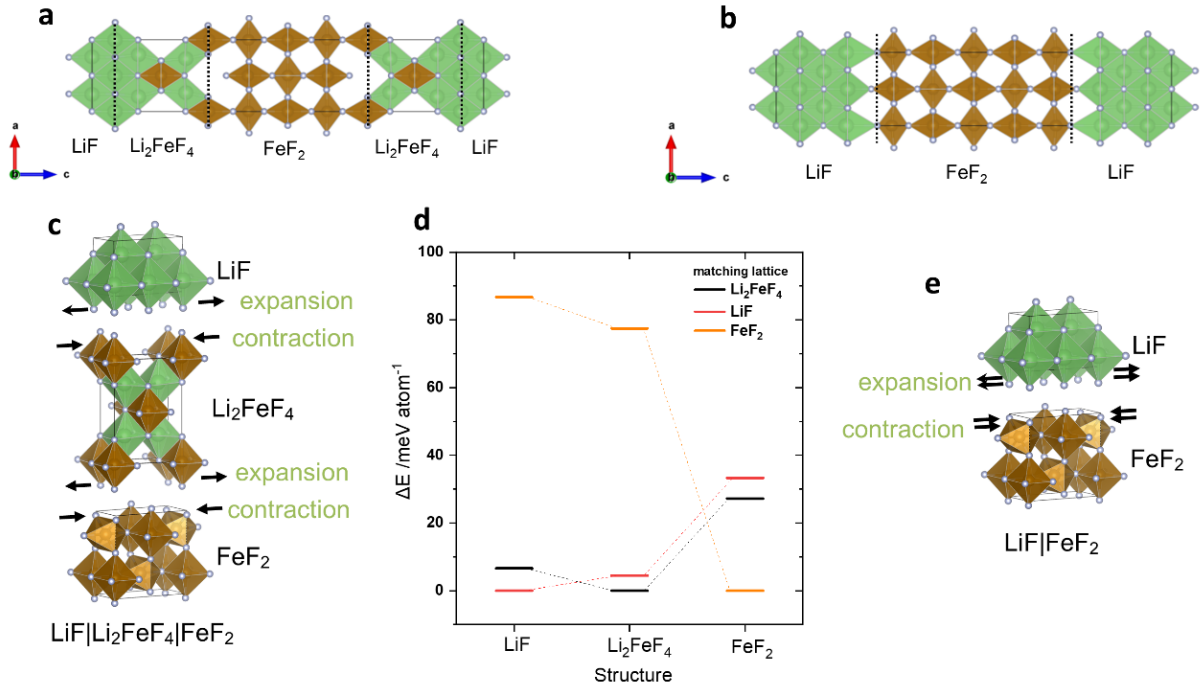

Figure S19. Structure comparison between **a)** the interface model "LiF|Li_2FeF_4|FeF_2" based on Li_2FeF_4 coherently connected (along its *c*-axis) with the LiF and FeF_2 units and **b)** the reference model "LiF|FeF_2" without the Li_2FeF_4 unit. **c)** Lattice matching condition of the "LiF|Li_2FeF_4|FeF_2" model. **d)** Energy increase due to lattice matching. **e)** Lattice matching condition of the "LiF|FeF_2" model. Both two interface models contain the same number of atoms and the same overall compositions. During the relaxation of the interface models, all degrees of freedom were allowed to change including lattice vectors and ion positions.

An interface model, denoted as "LiF|Li_2FeF_4|FeF_2", based on a Li_2FeF_4 interphase coherently connected to the LiF and FeF_2 units (Fig. 21a) was constructed. A "LiF|FeF_2" reference which excludes such interfacial Li_2FeF_4 unit (Fig. 21b) was also modelled for comparison. Based on our DFT computations on these two models, the "LiF|Li_2FeF_4|FeF_2" model is 22 meVÅ^{-2} (0.139 J m^{-2}) more stable than the "LiF|FeF_2" reference, suggesting that the inclusion of the Li_2FeF_4 interfacial component is energetically favoured.

Considering that LiF and FeF_2 suffer from significant lattice mismatch and the inclusion of the interphase may alter the energetics, we also evaluated the energies of relevant phases under lattice matching conditions. We found that epitaxial growth of LiF on FeF_2 (or vice versa) leads to considerable lattice strain and relatively large energy increase (33-86 meV atom^{-1}) (Fig. 21d-e). However, Li_2FeF_4 structure can be stretched/compressed to match the lattice constants of both LiF and FeF_2 with less energy increase (< 28 meV atom^{-1}) (Fig. 21c-d). These results suggest the interfacial Li_2FeF_4 may serve as a buffer between FeF_2 and LiF to relieve the strain originating from the significant lattice mismatch between the two end members—this is in line with our interpretation from a crystallographic perspective that the presence of Li_2FeF_4 mitigates the structural difference between LiF and FeF_2.

Section S10. NMF study of lithiated CuF_2

To determine whether the two-step topotactic phase transition is unique to FeF_2 rutile, we revisited our *in situ* PDF data on CuF_2 (distorted rutile $P2_1/n$)[6] using the same NMF approach (Movie S2). Surprisingly, we could also extract (at least) one additional component (Fig. S20a and S21), corresponding to orthorhombic Li_2CuF_4 (*Cmca*)[8] (Fig. S20b), whose PDF contribution was obscured in the difference pattern in our previous refinements. Inclusion of this intermediate phase in the refinement could significantly improve the fit (Fig. S22) and the results suggest that Li_2CuF_4 has an even smaller crystallite size (~ 1.0 nm) than Li_2FeF_4 in the lithiated FeF_2. This orthorhombic structure has Cu^{2+} in all vertex-shared positions, different from the edge-shared Fe^{2+} in Li_2FeF_4 (the difference likely stemming, at least in part, from the Jahn-Teller distortion of the Cu^{2+} ion), resulting in unique PDF fingerprints (Fig. 20b). Nevertheless, the structure relationship between the reactant/product and the orthorhombic intermediate remains evident and comparable with that in the lithiated FeF_2. This suggests lithiation of CuF_2 may also follow a topotactic *displacement* pathway.

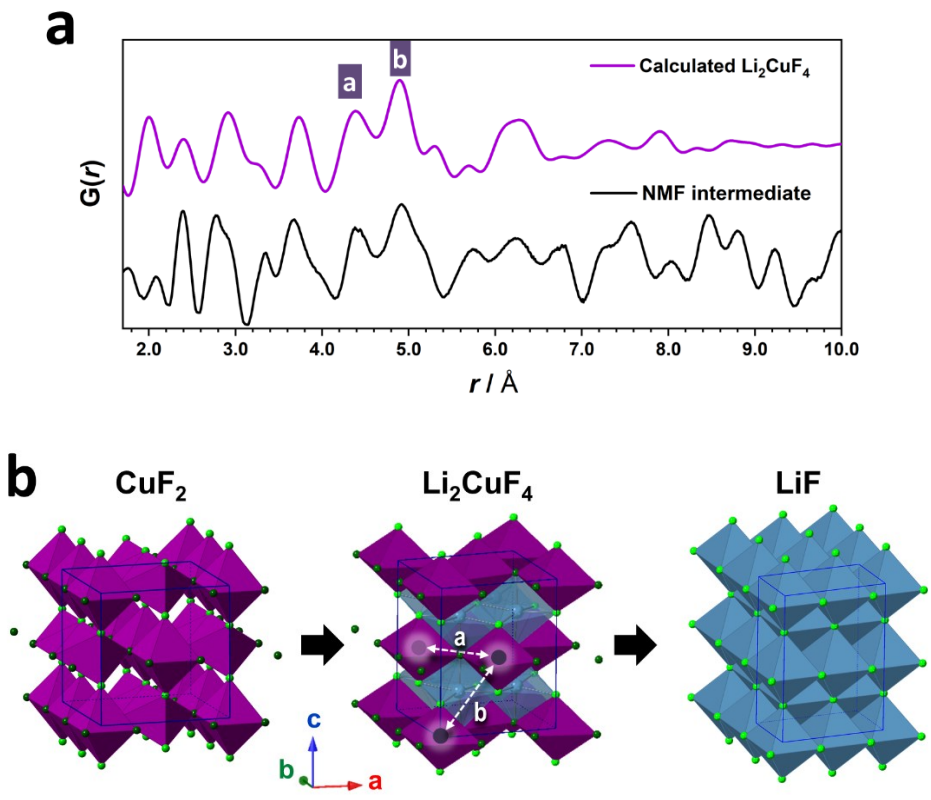

Figure 20. a) PDF comparison between the calculated pattern and the NMF-derived pattern for Li_2CuF_4 (*Cmca*) and **b)** the structures of the reactant (CuF_2), intermediate (Li_2CuF_4) and product (LiF) represented by the unit cell setting of Li_2CuF_4. Two corner-shared Cu pairs are indicated in both PDF pattern and structure by "a" and "b".

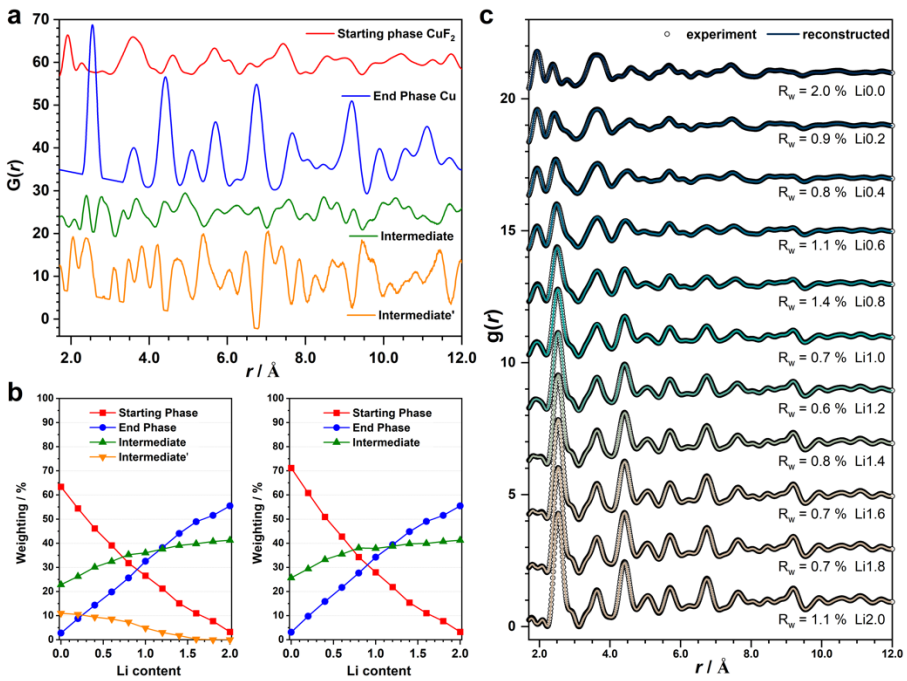

Figure S21. a) Four PDF components derived from the NMF analysis of the PDF data from the 1st discharge: Starting phase (CuF_2), End phase (Cu), Intermediate (Li_2CuF_4) and Intermediate' (dominated by a negative PDF contribution from Cu, possibly indicative of a non-uniform distribution of Cu particle sizes). **b)** The respective NMF-derived weightings of the four components and the adjusted weightings with contribution from the most minor component removed. **c)** Agreement between the experimental data and reconstructed PDF using NMF-derived output.

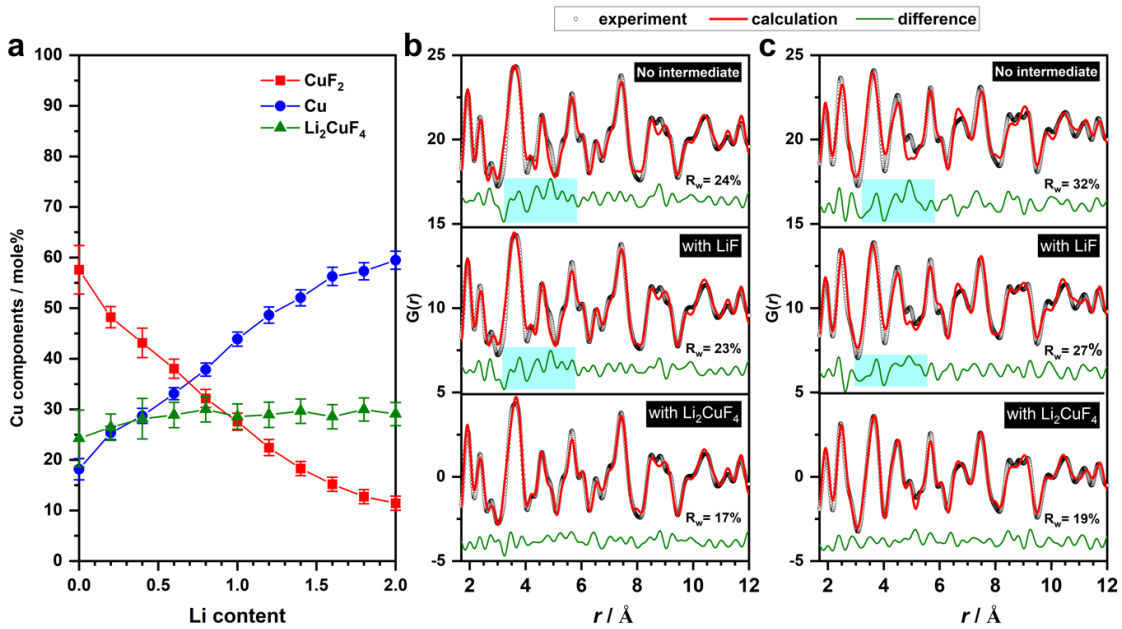

Figure S22. a) Phase evolution of the Cu-containing components derived from refinements of PDF data during the 1st discharge. PDF refinements of **b)** "dis Li 0.0" and **c)** "dis Li 0.4" CuF_2 data against various structure models: 1) without LiF and Li_2CuF_4, 2) including LiF in the refinement, and 3) including Li_2CuF_4 as an intermediate. The improvement of the fit due to the inclusion of the Li_2CuF_4 intermediate is evident. The discernible features due to the exclusion of the intermediate are highlighted in blue boxes.

Section S11. Radiation sensitivity of FeF_x

Metal fluorides are highly sensitive to the electron beam[9] − even under a short beam exposure (ca 10 s). For example, an earlier study of an n-FeF_2/C nanocomposite shows significant radiation-induced phase changes resulting in a Fe^{3+}-containing species (Fig. S23a), prior to its full reduction to Fe at longer irradiation times (180 s)[9]. Such radiation-induced phase behaviour was described as a disproportionation-like reaction of FeF_2 to form FeF_3 + Fe.[9] We note that a more recent (ex-situ) HRTEM study of the n-FeF_2 system observed the "disproportionation of FeF_2 to $LiFe^{2+}Fe^{3+}F_6$ + Fe" on lithiation of FeF_2[10]. In this study, a Fe^{3+}-containing trirutile $LiFe^{2+}Fe^{3+}F_6$ phase was proposed as the intermediate phase that occurs upon the lithiation of FeF_2, on the basis of electron energy loss spectroscopy (EELS) data (Fig. S23b).[10] Given the radiation sensitivity of FeF_2, the observation of Fe^{3+} upon lithiation (reduction) of FeF_2 cast doubt on the origination of this Fe^{3+} species, i.e., either within the electron microscope or from electrochemical lithiation.

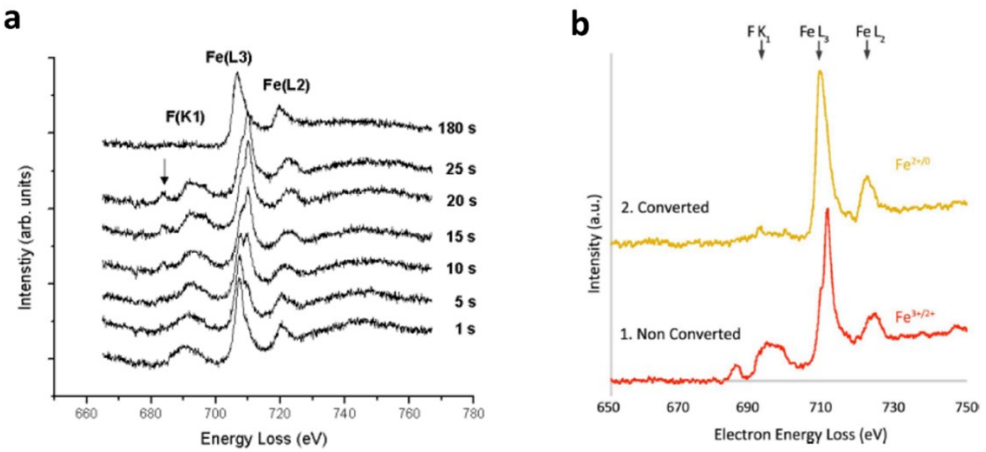

Figure S23. a) EELS spectra showing the effect of electron beam exposure time on the FeF_2 structure, adapted from Fig. 6 of Ref 9 (with permission). **b)** EELS spectra of discharged FeF_2, adapted from Extended Data Fig.2 in Ref 10.

To clarify our doubt, we carefully examined the FFT results (derived from the HRTEM data) presented in Ref 10. Our examination shows that the simulated ED pattern using the model proposed in Ref 10 does not match their own experimentally derived FFT data. Note that both rutile and trirutile show (00*l*) (*l* = odd) systematic absences. These absences were clearly marked by black square in Ref 10. We have particularly highlighted the $(001)_{FeF2}$ and $(003)_{LiFe2F6}$ absences using red arrows (Fig. S24c-d). Given the structural coherence between rutile and trirutile phases, their coexistence in the same fluoride sublattice would lead to absent reflections corresponding to $(001)_{FeF2}$ and $(003)_{LiFe2F6}$ in a similar position to that shown by the red arrow in their superimposed ED simulations (Fig. S24a) − this contradicts the experiment where one strong reflection is present in that position as marked by yellow circles in Fig. S24b. This contradiction demonstrates a symmetry change in the intermediate's structure (*i.e.* removal of the screw axis), which indicates that the intermediate is not a trirutile, given that trirutile has the same symmetry as rutile. By contrast, our Li_2FeF_4 structure model − with the removal of 4_2 axis and the preservation of mirror planes ($P4_2/mnm \rightarrow Cmmm$) – provides an excellent match to their experimental data (Fig. S24e). Finally, we note that the experimental FFT data of pure-FeF_2 in Ref 10 (e.g. Fig. S20 of Ref 10) exhibits a (001) reflection, which should not be present due to a systematic absence. We therefore suggest that the Fe^{3+} observed in Ref 10, which indirectly indicated the presence of a trirutile structure, was more likely to originate from radiation damage. Finally, we note that the $LiFe_2F_4$ proposed in this work is supported by bulk structural methods (PDF) that do not suffer from similar degradation processes. No evidence for trirutile emerged from the PDF studies.

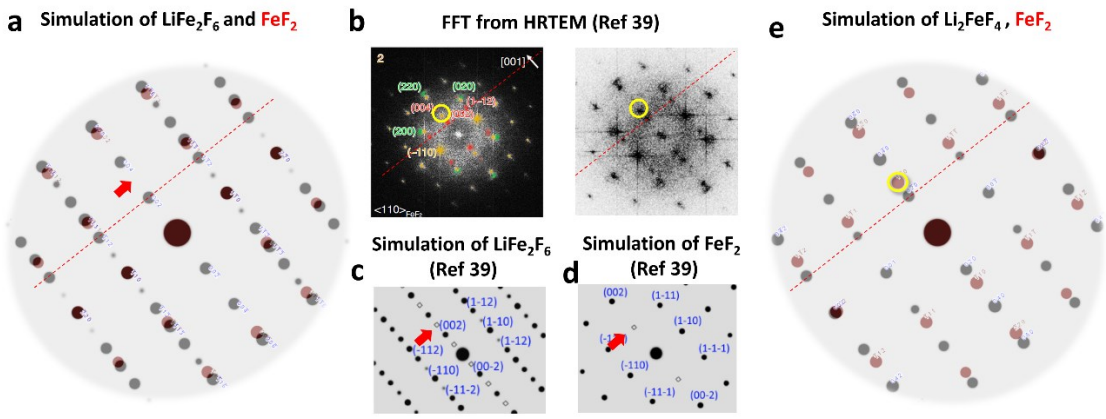

Fig. S24 a) Superposition of the ED pattern simulated using the trirutile $LiFe_2F_6$ (black) and FeF_2 (red) structures viewed from the perspective indicated in Ref 10. **b**) FFT data with different contrast adapted from Ref 10 (Fig. 4 stage 2 and Fig. S21 in Ref 10), in which yellow and red spots respectively denote FeF_2 and $LiFe_2F_6$ reflections. Yellow circles mark the diffraction spots which were assigned to FeF_2 in Ref 10 but were absent in the simulated data shown in c and d due to systematic absences. **c)** and **d)** respectively correspond to simulated ED data of $LiFe_2F_6$ and FeF_2 structures adapted from Ref 10 (Fig. S21 in Ref 10) in which systematic absences are marked by black square. Red arrows indicate the specific absence which contradicts the data (marked by yellow circle in b). **e)** Superposition of the ED pattern simulated using our model Li_2FeF_4 (black, viewed from [100] axis) and FeF_2 (red). Yellow circles mark the diffraction spot consistent with the experimental data shown in b). Dashed lines are added to assist the visual comparison.

REFERENCES

1 Müller, U. *Symmetry relationships between crystal structures: applications of crystallographic group theory in crystal chemistry*. Vol. 18 (OUP Oxford, 2013).

2 Hattori, T., Matsuda, T., Tsuchiya, T., Nagai, T. & Yamanaka, T. Clinopyroxene-perovskite phase transition of $FeGeO_3$ under high pressure and room temperature. *Phys. Chem. Miner.* **26**, 212-216 (1999).

3 Badway, F., Pereira, N., Cosandey, F. & Amatucci, G. G. Carbon-Metal Fluoride Nanocomposites: Structure and Electrochemistry of FeF_3 : C. *J. Electrochem. Soc.* **150**, A1209-A1218 (2003).

4 Rauch, E. *et al.* Automatic crystal orientation and phase mapping in TEM by precession diffraction. *Microscopy and Analysis* **22**, S5-S8 (EU) (2008).

5 Lee, S. *et al.* Weak-ferromagnetism of CoF_3 and FeF_3. *Physica B Condens. Matter* **551**, 94-97 (2018).

6 Hua, X. *et al.* Comprehensive Study of the CuF_2 Conversion Reaction Mechanism in a Lithium Ion Battery. *J. Phys. Chem. C* **118**, 15169-15184 (2014).

7 Yamakawa, N., Jiang, M., Key, B. & Grey, C. P. Identifying the Local Structures Formed during Lithiation of the Conversion Material, Iron Fluoride, in a Li Ion Battery: A Solid-State NMR, X-ray Diffraction, and Pair Distribution Function Analysis Study. *J. Am. Chem. Soc.* **131**, 10525-10536 (2009).

8 P Jain, A. *et al.* Commentary: The Materials Project: A materials genome approach to accelerating materials innovation. *APL Materials* **1**, 011002 (2013).

9 Cosandey, F., Al-Sharab, J. F., Badway, F., Amatucci, G. G. & Stadelmann, P. EELS Spectroscopy of Iron Fluorides and FeF_x/C Nanocomposite Electrodes Used in Li-Ion Batteries. *Microsc. Microanal.* **13**, 87-95 (2007).

10 Xiao, A. W. *et al.* Understanding the conversion mechanism and performance of monodisperse FeF_2 nanocrystal cathodes. *Nat. Mater.* **19**, 644-654 (2020).